A&A 626, A35 (2019)
https://doi.org/10.1051/0004-6361/201935291

Astronomy & Astrophysics

The young stellar population in NGC 247

Main properties and hierarchical clustering*

M. J. Rodríguez[1], G. Baume[1,2], and C. Feinstein[1,2]

[1] Instituto de Astrofísica de La Plata (CONICET-UNLP), Paseo del bosque s/n, La Plata B1900FWA, Argentina
e-mail: jimenaro@fcaglp.unlp.edu.ar
[2] Facultad de Ciencias Astronómicas y Geofísicas – Universidad Nacional de La Plata, Paseo del bosque s/n, La Plata B1900FWA, Argentina

Received 16 February 2019 / Accepted 4 April 2019

ABSTRACT

Aims. We seek to investigate the characteristics of the young stellar population in the spiral galaxy NGC 247. In particular, we focused our attention in its hierarchical clustering distributions and the properties of the smallest groups.
Methods. We used multiband *Hubble* Space Telescope (HST) data from three fields covering more than half of NGC 247 to select the young population. Then, through the path linkage criterion (PLC), we found compact young star groups and estimated their fundamental parameters, such as their stellar densities, sizes, number of members, and luminosity function (LF) slopes. We also performed a fractal analysis to determinate the clustering properties of this population. We built a stellar density map and dendrograms corresponding to the galactic young population to detect large structures and depict their main characteristics.
Results. We detect 339 young star groups, for which we compute a mean radius of ∼60 pc and a maximum size distribution between 30 and 70 pc. We also obtain LF slopes with a bimodal distribution showing peaks at ∼0.1 and ∼0.2. We identify several candidates for HII regions that follow an excellent spatial correlation with the young groups found by the PLC. We observe that the young populations are hierarchically organized, wherein the smaller and denser structures are within larger and less dense structures. We notice that all these groups present a fractal subclustering, following the hierarchical distribution observed in the corresponding stellar density map. For the large young structures observed in this map, we obtain a fractal dimension of ∼1.6–1.8 using the perimeter-area relation and cumulative size distribution. These values are consistent with a scenario of hierarchical star formation.

Key words. stars: early-type – stars: luminosity function, mass function – galaxies: individual: NGC 247 – galaxies: star formation – galaxies: star clusters: general

1. Introduction

Most massive stars do not form in isolation, rather they take shape in embedded clusters (Lada & Lada 2003). Therefore, these young star groups constitute the fundamental blocks of star formation in galaxies. Their study is essential to understand star formation processes in the host galaxy as well as its recent history.

Different young stellar groups are found at diverse scales, from young compact open clusters to important stellar complexes of hundreds of parsecs, going through OB associations and various stellar aggregates. All these young structures are not independent of each other; they are linked in a hierarchical way in which the most compact and dense structures are within larger and less dense structures (e.g., Elmegreen & Efremov 1996; Efremov & Elmegreen 1998). Thus, the OB associations host stellar subgroups and open clusters (Blaauw 1964) and at the same time these associations are part of a larger and looser stellar aggregate (Rodríguez et al. 2018, 2016). It is usually accepted that this hierarchical behavior is inherited from their parent molecular clouds (e.g., Elmegreen & Salzer 1999). The interstellar molecular gas presents a self-similar distribution known as a fractal structure, which seems to be driven mainly by turbulence and self-gravity (Elmegreen & Efremov 1996; Elmegreen 1999).

In this way, star formation proceeds continuously along several scales (Gouliermis 2018). Thus, it seems arbitrary to set boundaries on the different groups (clusters, OB associations, aggregates, complexes, and supercomplexes) based only on their morphology. However, such separation is useful to study young stellar populations at different scales and be able to establish their characteristics.

In this work we present a study of the young stellar population in the Sculptor group spiral galaxy NGC 247. This galaxy is catalogued as a SAB(s) d D (Konstantopoulos et al. 2013), is located near the south Galactic pole (l = 113.95°; b = −83.56°), has a high inclination angle (i = 74°; Schaap et al. 2000), and an estimated distance of 3.6 Mpc (García-Varela et al. 2008).

Several studies have been carried out on NGC 247 using ground-based observations. Davidge (2006) reported the presence of an extended stellar disk with star formation using deep visible and near-infrared images and derived a star formation rate of 0.1 $M_\odot$ yr^{-1} in the last 16 Myr. Carignan & Puche (1990) studied the properties of this galaxy in HI using Very Large Array observations. These authors found a relatively compact HI envelope compared to other systems. On the other hand, Ferguson et al. (1996) noted that the H$_\alpha$ emission was mainly from two spiral arms and found a small total H$_\alpha$ flux compared to other spirals and irregulars galaxies.

* Full Table 3 is only available at the CDS via anonymous ftp to cdsarc.u-strasbg.fr (130.79.128.5) or via http://cdsarc.u-strasbg.fr/viz-bin/qcat?J/A+A/626/A35

In spite of the proximity of NGC 247, detailed studies have not been carried out about its stellar population. There are no catalogs of stellar associations and there are only records of a few identified clusters in the literature. Larsen (1999) identified three massive star clusters in NGC 247, but only one of these was associated with a blue, and therefore young, population. Olsen et al. (2004) detected three globular clusters, and Tao et al. (2012) reported the existence of a young stellar association close to an ultraluminous X-ray source using visible HST and *Chandra* X-ray observations.

In this paper, we took advantage of the excellent quality data obtained with the *Hubble* Space Telescope (HST), to study the young stellar population of NGC 247 for the first time. We focused mainly on the young star groups, obtaining their principal characteristics, and on the study of the hierarchical organization observed in the young population.

This work is organized as follows. In Sect. 2 we describe the observations and photometry data used in this research. In Sect. 3 the methods used to identify the young stellar population and to search for stellar groups inside this population are described. In Sect. 4 we describe the principal characteristics of the detected groups. The detection of larger young structures is described in Sect. 5. A morphological analysis of the detected groups and structures is presented in Sect. 6. Finally, in Sect. 7 we present our conclusions.

2. Data

2.1. Observations

In this work we used images obtained with the Wide Field Camera (WFC) of the Advanced Camera for Surveys (ACS). These images correspond to three fields in NGC 247, which cover a total length of ∼10′ encompassing the southern half of the galaxy (see Fig. 1). Each field was observed using the broadband HST filters $F475W$, $F606W$, and $F814W$.

The observations were carried out in September 2006 during the HST Cycle 15 as part of the program GO-10915 (PI: J. Dalcanton). The observation details are listed in Table 1. The WFC has a mosaic of two CCD detectors with a field of view of 3.3′ × 3.3′ and a scale of 0.049″ pixel^{-1}. The observation described above were acquired from the *Hubble* Legacy Archive[1].

2.2. Photometry

The photometry data used in this work was obtained from the MAST database of the Space Telescope Institute (STScI)[2]. These data correspond to the "star files" of the *ACS* Nearby Galaxy Survey (ANGST).

The point spread function photometry was carried out by Dalcanton et al. (2008), using the software DOLPHOT[3] adapted for the ACS camera (Dolphin 2000). The files mentioned above contain the photometry of all objects classified as stars with good signal-to-noise values ($S/N > 4$) and data flag <8.

In Fig. 2 we show the photometric errors in the various bands corresponding to the objects classified as stars in the three fields. We built the $F606W$ luminosity function (LF) for the three fields (see Fig. 3) to evaluate the completeness of the data. We can see in Fig. 3 that the number of stars per bin starts to decrease at $F606W \sim 27.5$. Therefore we considered that the sample is complete up to this value.

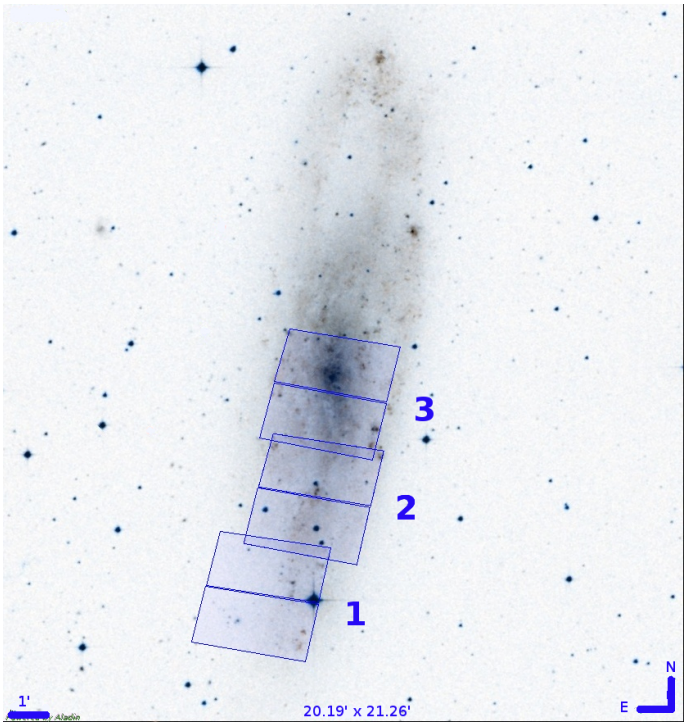

Fig. 1. Distribution of the different HST/ACS fields (rectangles) used in this work overlaid on a Digitized Sky Survey (DSS) image of NGC 247. North is up and east is left; the image cover 20.19′ × 21.26′.

Table 1. Observations details.

Field	Band	N_{exp}	t_{exp} [s]	Date
1	$F475W$	3	2253	09-22-2006
1	$F606W$	3	2280	09-22-2006
1	$F814W$	3	2250	09-22-2006
2	$F475W$	2	1480	09-20-2006
2	$F606W$	2	1507	09-20-2006
2	$F814W$	2	1534	09-20-2006
3	$F475W$	2	1480	09-21-2006
3	$F606W$	2	1507	09-21-2006
3	$F814W$	2	1534	09-21-2006

2.3. Photometric correlation of tables

The ANGST provides photometric tables with the information of only two bands. To join the three magnitudes in a single table for field, we used the code STILTS[4] to perform a cross-correlation (with logical "OR") between tables with $F606W-F475W$ bands and those with $F814W-F606W$ bands; we obtained three photometric tables, one for each field.

As we note in Fig. 1, the adjacent fields slightly overlap each other. We used STILTS to merge the information of the three fields into one single table with approximately 1.3×10^6 objects. In this procedure we used only the brightest objects ($F606W <$ 24). We first compared the astrometric information with objects of Frame 3 in common with *Gaia* DR2 and we found a small systematic difference that was corrected. Then we compared

[1] http://hla.stsci.edu/
[2] https://archive.stsci.edu/
[3] http://americano.dolphinsim.com/dolphot/
[4] http://www.star.bris.ac.uk/~mbt/stilts/

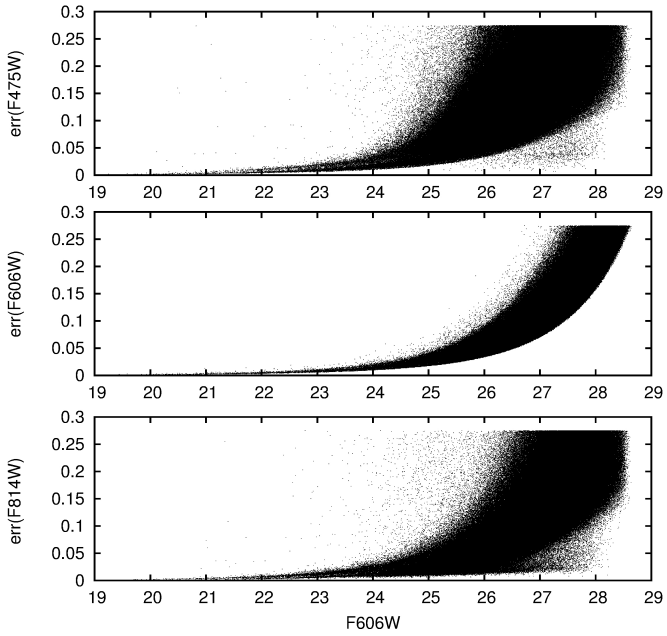

Fig. 2. Photometric errors in the different bands.

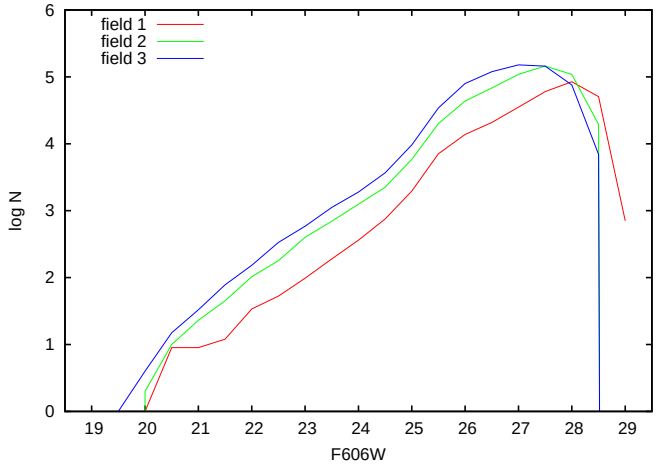

Fig. 3. Luminosity function for the three studied fields.

the astrometric and photometric data of the objects in the overlapped regions and we found small differences in the astrometry but not important differences (Δmag $\sim$ 0.01) in their photometry values. Finally, we adopted the central part of NGC 247 (Frame 3) as a reference and we carried out coordinates of Frames 1 and 2 to the former. For objects in overlapped regions, after the calibration we took the average of data between the stars in each field. The computed astrometric differences are presented in Table 2.

2.4. Stellar blend and foreground contamination

Star blends can be found in cases in which two (or more) stars do not have the same center but are close enough to be considered as one object. The software used to measure the photometry of the stars (DOLPHOT) gives as a result for each object the sharpness, the crowding, the S/N, and the χ^2 of the point spread function fitting. These parameters are a good estimator of the quality of the measurement and a reference for detecting blended stars. The most problematic case is when two stars that could be centered at the same position of a pixel and mistakenly detected by the photometry software as only one star. We could not identify these stars by photometry or other means, but we can modeled the severity of the effect of this overlap.

Table 2. Astrometric corrections applied ACS/HST data.

Fields	$\Delta\alpha[''] $	$\Delta\delta[''] $	N
3-*Gaia*	0.586 ± 0.071	−0.030 ± 0.025	63
2-3	−0.172 ± 0.058	0.082 ± 0.040	76
1-2	0.312 ± 0.002	0.110 ± 0.004	12

Notes. Values are given as mode ± stdev and N indicate the number of objects used in each case.

An estimation of the maximum level of blending can be calculated by measuring the maximum star density in the galaxy and assuming that this stellar density is constant over the whole object. Thus, we can model the blending, considering that the stars are distributed with a Poisson distribution. This is equivalent to the procedure of Kiss & Bedding (2005), which is discussed deeply for these kinds of observations in Feinstein et al. (2019). Therefore, this model allows us to obtain an upper limit of probability of blends for the crowded regions that is larger than the probability of the less populated places. By this procedure we obtained that the probability of losing stars by blends is less than 2% in more crowded locations. So, we do not consider blending as an important issue in this work.

One possible source of data contamination could be the galactic stars in the field of view of NGC 247. However, this galaxy has galactic coordinates $l = 113.95°$; $b = -83.56°$, which locates the galaxy close to the south pole of the Milky Way and far away from the disk and the galactic center. This means that the probability of contamination of our sample by blue galactic stars is negligible. In order to recheck this possible contamination we ran several simulations with the Besançon model of the galaxy[5] and also with the Trilegal[6] (Girardi et al. 2012) model. In both cases we found that in very few models we got at least one blue Milky Way star for an area equivalent to the observed fields. So, we do not consider the galactic contamination as a problem for the analysis of young blue stars

3. Search of young stellar groups

3.1. Identification of the various star populations

In the top panel of Fig. 4 we show a combination of a Hess and color magnitude diagram (CMD) for the detected objects in the studied region of NGC 247, where the different colors indicate densities ranging from blue (lower densities) to red (higher densities). In this figure, it is possible to note two different populations. The left sequence is shown to reach magnitudes close to $F606W \sim 19$, which is associated with a young population, and the right sequence corresponds to a more evolve population. Taking this into account, we adopted the following criteria to separate the different stellar populations:

– Bright stars: $F606W < 25$
– Blue stars:
$(F475W-F606W) < 0.3$ and $(F606W-F814W) < 0.3$
– Red stars:
$(F475W-F606W) > 0.6$ and $(F606W-F814W) > 0.6$

[5] https://model.obs-besancon.fr/
[6] http://stev.oapd.inaf.it/cgi-bin/trilegal

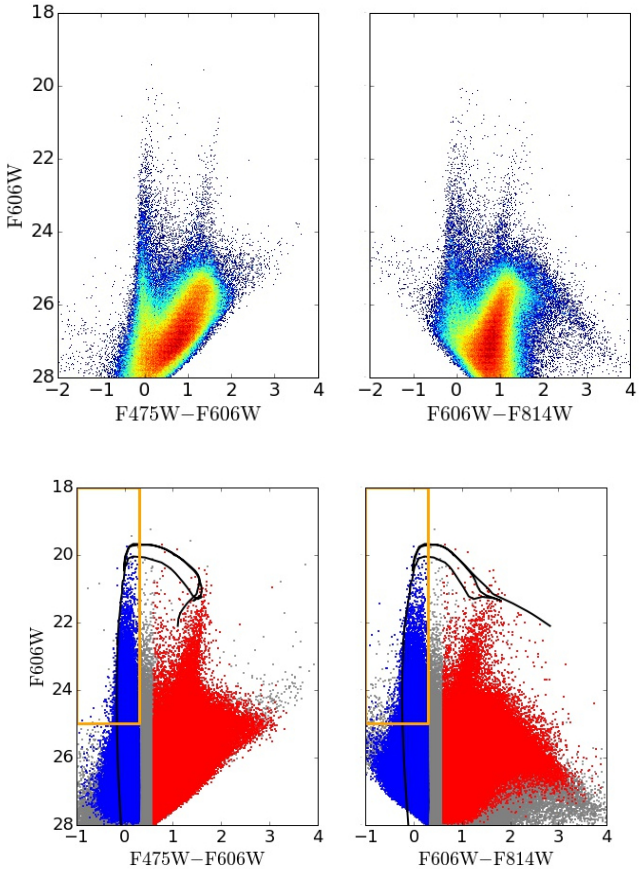

Fig. 4. *Top panel*: combination of Hess diagram and CMDs for the detected objects in the three observed fields. The different colors indicate densities, ranging from blue (lower densities) to red (higher densities). The diagrams correspond to the color indexes $F475W-F606W$ and $F606W-F814W$ at *left* and *right*, respectively. *Bottom panel*: same CMDs that are shown in the *top panel*, but we separate the blue and red populations with blue and red, respectively. The orange rectangle encloses the bright blue stars; we use this selection to search the young stellar groups. In this figure we overlapped the PARSEC version 1.2S isochrone (Tang et al. 2014) corresponding to 10^7 years and metallicity $Z = 0.0152$. This model was displaced, adopting a distance modulus of $(V_0 - M_V) = 27.78$ (García-Varela et al. 2008), a normal reddening law ($R = A_V/E(B-V) = 3.1$), and a value for $E(B-V) = 0.015$, corresponding to the foreground reddening toward NGC 247 (Schlafly & Finkbeiner 2011).

In the bottom panel of Fig. 4 we indicate the blue and red populations in blue and red, respectively, derived from the above criteria. The rectangle encloses the blue bright stars, which are used to identify young stellar groups with the PLC method as described below. In this figure we overlapped the PARSEC version 1.2S evolutionary model (Tang et al. 2014) corresponding to 10^7 years and metallicity $Z = 0.0152$, to make a comparison with a young stellar population. This isochrone was displaced adopting a distance modulus of $(V_0 - M_V) = 27.78$ (García-Varela et al. 2008), a normal reddening law ($R = A_V/E(B-V) = 3.1$) and a value for $E(B-V) = 0.015$, corresponding to the foreground reddening toward NGC 247 (Schlafly & Finkbeiner 2011). The following coefficients were used to transform these values to the HST system: $A_{F475W}/A_V = 1.192$, $A_{F606W}/A_V = 0.923$, and $A_{F814W}/A_V = 0.605$[7] (O'Donnell 1994).

[7] http://stev.oapd.inaf.it/cgi-bin/cmd

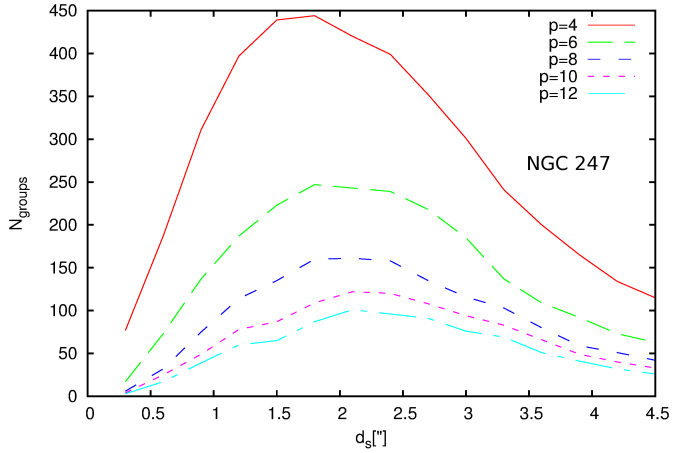

Fig. 5. Number of stellar groups detected with the PLC as a function of the search radius d_s for multiple values of p.

In both panels is possible to note that the main sequence population is very well delineated by a thin line of blue stars. This fact suggests that differential extinction in this galaxy would be negligible. In order to check this, we compared the position in the CMD diagrams of all the bright stars that were not intrinsically red ($F475W-F606W < 1$) with the theoretical model of 10^7 years, shown in the bottom panel of Fig. 4. Following the procedure used in Rodríguez et al. (2018), we estimated individual absorption values for these stars. We found low values of A_V with a mode of 0.1 mag and a mean value of 0.2 mag in their distribution. According to these results, we considered that the effects of the differential extinction in this galaxy is negligible for the detection of young groups.

3.2. Searching method

We used the Path linkage criterion (PLC; Battinelli 1991) over the bright blue population to detect young stellar groups in the galaxy. The applied procedure was explained in our previous works (Rodríguez et al. 2018, 2016). The PLC is an agglomerative friend of friend algorithm that links stars of the bright blue sample using a search radius d_s and considers a minimum number of stars (p) to define a stellar association. In the Fig. 5 we show the number of stellar groups detected as a function of d_s for different p values. We can see that independent of the value of p the maximum of the distribution falls around 2 arcsec. This maximum corresponds to the optimal value of d_s according to Battinelli (1991). We decided to adopt a range of d_s values between 0.3–2.0 arcsec (5–35 pc), and in this way we ensure that we are not losing the smallest groups. The PLC method starts the search with $d_s = 0.3$ arcsec. Then, the stars belonging to the detected groups are deleted from the sample and the PLC runs again increasing the value d_s in a step of 0.4 arcsec. This procedure is repeated until d_s reaches the value of 2 arcsec. We also considered from the results shown in Fig. 5 that $p = 8$ stars is an adequate value. Using this method we detected 339 young stellar groups.

It is important to note that although the PLC method is devised to detect stellar associations, we cannot rule out that some open clusters or stellar aggregates larger than a typical association are detected. For this reason, "stellar groups" refers to all the groups detected, although it is expected that the most of these are stellar associations.

Table 3. Main parameters of young stellar groups in NGC 247.

(1) Name	(2) α_{2000} δ_{2000}	(3) d_{GG} [Kpc]	(4) r [pc]	(5) N_g N_{bg}	(6) N_d N_{bd}	(7) $F606W_{min}$	(8) ρ [obj./pc^3]	(9) Γ e_Γ	(10) $\overline{m}$ $e_{\overline{m}}$	(11) $\overline{s}$ $e_{\overline{s}}$	(12) Q e_Q
AS001	00:47:13.4	10.28	11.87	22	22	21.24	0.00129	0.05	0.74	0.93	0.79
	−20:51:40.5			9	9			0.04	0.08	0.08	0.09
AS002	00:47:08.8	6.66	11.52	18	14	21.27	0.00156	0.02	0.72	0.90	0.80
	−20:50:54.7			10	10			0.07	0.09	0.09	0.08
AS003	00:47:08.7	0.99	10.82	25	12	22.19	0.00170	0.07	0.83	1.09	0.76
	−20:44:45.8			9	9			0.25	0.09	0.09	0.10
AS004	00:47:10.1	4.96	19.20	66	49	21.02	0.00115	0.05	0.62	0.92	0.67
	−20:48:55.7			34	34			0.05	0.04	0.04	0.06
AS005	00:47:15.9	8.11	10.12	21	14	21.71	0.00184	0.04	0.74	0.95	0.78
	−20:47:40.5			8	8			0.09	0.09	0.09	0.10
AS006	00:47:07.6	0.70	11.17	23	18	22.83	0.00120	0.04	0.72	0.97	0.75
	−20:45:56.0			7	7			0.23	0.09	0.09	0.09
AS007	00:47:10.3	5.04	45.73	342	160	20.32	0.00019	0.13	0.57	0.73	0.78
	−20:48:56.2			77	77			0.05	0.03	0.03	0.06
AS008	00:47:10.5	5.26	71.56	869	261	20.12	0.00004	0.15	0.47	0.81	0.57
	−20:49:00.1			57	57			0.06	0.03	0.03	0.06
AS009	00:47:08.4	0.09	40.14	323	46	20.60	0.00006	0.12	0.54	0.80	0.67
	−20:45:35.3			25	16			0.06	0.04	0.04	0.08
AS010	00:47:04.4	3.84	45.38	350	66	20.34	0.00010	0.14	0.51	0.71	0.72
	−20:45:15.8			39	39			0.06	0.04	0.04	0.06

Notes. Columns: (1): Identification. (2): Equatorial J2000 coordinates. (3): Galactocentric distance. (4): Radius. (5): Total number of stars (N_g) and number of *bright blue* stars (N_{bg}) inside the group radius. (6): Total number of stars (N_d) and number of *bright blue* stars (N_{bd}) inside the group radius after field decontamination. (7): $F606W$ value of the brightest blue star. (8): Stellar density. (9): LF slope (Γ) and its error (e_Γ). (10): Mean edge length in a MST ($\overline{m}$) and its error ($e_{\overline{m}}$). (11): Mean separation of the stars in the group ($\overline{s}$) and its error ($e_{\overline{m}}$). (12): Q parameter and its error (e_Q). We present the first ten groups; the complete table is only available at the CDS.

3.3. Detection of stochastic fluctuations

We performed numerical simulations using a random distribution of stars with similar densities of those found in the densest areas of the galaxy (ρ = 0.185 stars arcsec^{-2}) and we ran the PLC over these. These experiments allowed us to estimate the fraction of the PLC stellar groups that should not be real, but only stochastic fluctuations of field stars. We did not detect any groups in 10 000 experiments with the smallest search radius (d_s = 0.3 arcsec); with d_s = 0.7 arcsec we found only 5 groups in 10 000 experiments and we found 424 groups with d_s = 1 arcsec. These fractions are very small, which strengthens the veracity of the groups detected in the previous section.

4. Parameters of the PLC groups

The 339 PLC groups were studied in a homogeneous and systematic way by means of our own numerical code through which we could estimate the fundamental parameters of the groups. To estimate the coordinates and size of the groups, we derived the mean and standard deviation values of the individual positions of the stars identified by the PLC method on each group. Therefore, mean values were adopted as their corresponding centers and twice the standard deviation as the radius (R) of a circle enclosing each group. The obtained values are presented in the first columns of Table 3. The size distribution of the groups is presented in Fig. 6 (panel a), in which we note a large range of radii from 10 pc to 200 pc. The mode in the distribution is about 30–70 pc and has a mean value of ∼60 pc. This values are somewhat larger that those found in our previous works for NGC 300 and NGC 253 (Rodríguez et al. 2018, 2016). In the former we found a peak in the size distribution and a mean radius of 25 pc, but it must be considered that in that case we adopted the radius as 1σ instead of 2σ (as in the present work). Considering $R = 2\sigma$, we obtained a mean and a mode of 50 pc, which is a bit lower that the value found in NGC 247 but is still consistent. For NGC 253 we found even lower values that have a mode of 40 pc and a mean radius of 47 pc. In the literature lower values were found too. For example, Drazinos et al. (2016) estimated a mean radius of ∼30–35 pc for the young associations in four Local Group galaxies (SMC, M31, M33, and NGC 6822) using a friend-of-friend algorithm. Drazinos et al. (2013) found a mean size between 62 and 75 pc (radius of ∼31–38 pc) for the associations in the galaxies NGC 925, NGC 2541, NGC 3351, NGC 3621, NGC 4548, and NGC 5457. On the other hand, a wider range of sizes were found by Battinelli et al. (2000), who studied the young stellar groups in the galaxies NGC 2717, NGC 1058, and UGC 12732; these authors found values for the radius mode between 25 and 50 pc and between 52 and 89 pc for the mean radius. Battinelli (1991) derived a mean radius of 45 pc for the OB associations in the SMC, this value is larger than the value found by Drazinos et al. (2016) for the same galaxy. In our Galaxy, Melnik & Efremov (1995) found still lower values for the OB association sizes in the solar vicinity with a mode value of 15 pc and an average radius of 20 pc.

Subsequently, we built their corresponding decontaminated CMDs, statistically deleting the field objects located in the CMDs of each group region. This procedure was based on the steps given by Baume et al. (2003). That is, we built the histograms of objects in a three-dimensional space of $F606W$, $F434W-F606W$, and $F606W-F814W$ coordinates for each group and for its corresponding comparison field, then both

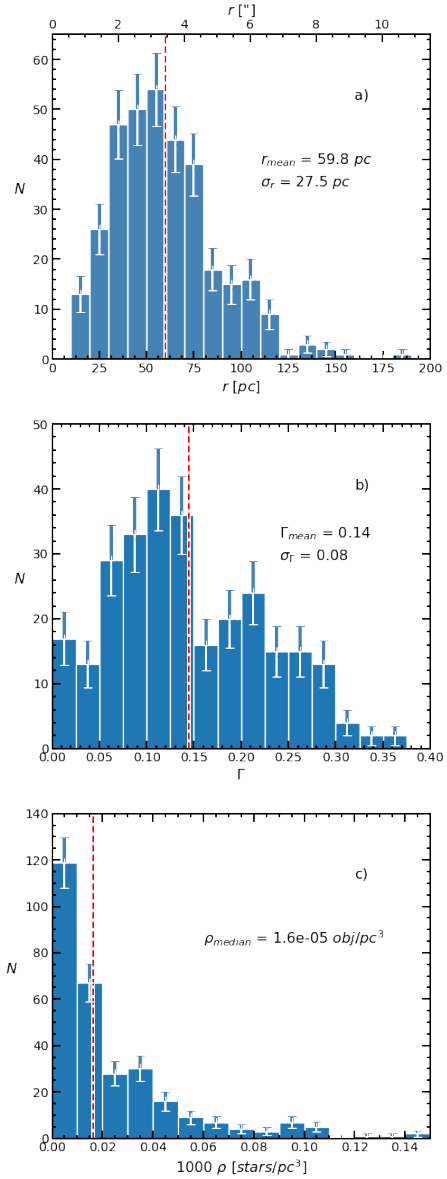

Fig. 6. Distribution of sizes (*panel a*), Γ values (*panel b*), and volumetric densities (*panel c*) of the young groups found by the PLC. Error bars arise from the Poisson statistics ($\sqrt{N}$). Dashed vertical lines indicate mean or median values.

histograms were subtracted. The adopted bin were 0.2 mag wide in magnitude and 0.1 mag in each color. We adopted a circular regions with the corresponding previous computed radius for each stellar group. For the comparison fields we considered an annular shape with an inner and outer radius given by $r1$ and $r2$ times the corresponding radius of the stellar group. To select a clean comparison field, we chose $r1 = 1.5$ and we avoided those regions corresponding to detected nearby young groups to that under study, therefore the chosen $r2$ value was a value between 2 and that corresponding to a comparison field with at least 100 objects. Since the adopted stellar group region and its corresponding field region cover different sky areas, the field histogram was weighted, before the subtraction, by the amount of red stars in both regions. To minimize the amount of unreliable subtractions, this procedure was applied over all the cases for which the number of blue objects after the subtraction was larger than the square root of the number of blue object before it. Finally, the decontaminated CMD of each group was generated with random objects following the shape of the resulting three-dimensional histogram.

Next, based on the previously obtained decontaminated CMDs, we built their corresponding LFs for all and for blue bright objects and computed the amount of blue objects (N_b) of each group. In particular, we also performed a power-law fit over the LFs of blue objects and estimated their corresponding Γ parameter considering only the brightest region ($F606W < 26$). In Fig. 7 we present the $F606W$ versus $F475W-F606W$ for the circular region of five detected young stellar groups together with those CMDs from their corresponding comparison fields. We also present the obtained subtracted CMDs and the associated LFs for the $F606W$ band (see figure caption for details). The corresponding distribution of values of the slopes is presented in Fig. 6b, where most of the values spread from 0.05 to 0.30; this distribution has a bimodal shape with maxima at $\Gamma \sim 0.1$ and ∼0.2. These facts could be understood as the different behavior of two stellar populations with differences in age, metallicity, and/or the initial mass functions (IMFs). As was already indicated, the general CMDs of NGC 247 (see Fig. 4) show a well-defined location for main sequence stars and blue helium burning stars, therefore the effect of different metallicity would be placed as a second order term. The same can be established for the initial mass distribution effect, since these low slope groups do not have preferential location in the galaxy. Therefore, we considered that the bimodal behavior of the Γ is mainly due to age differences. In particular, the second peak in the distribution is comparable with the values found in the literature. Rodríguez et al. (2018) found a mean value of 0.21 for the LF slope in NGC 253. For open cluster in our Galaxy, Kharchenko et al. (2009) found a LF slope between 0.2 and 0.3, while Phelps & Janes (1993) derived a bit larger value of 0.34.

Additionally, we computed the volumetric density of the stellar groups taking into account the number of decontaminated bright blue objects in an spherical volume with radius R. We found then the distribution presented in Fig. 6c, which has a median value of $\rho = 1.6 \times 10^{-5}$ stars pc^{-3}. This value was estimated considering only bright objects ($F606W < 25$), which correspond to approximately B1 spectral type.

In Table 3 we present the first ten rows of the resulting catalog, in which the properties for each of the 339 young groups are listed. The complete version is only available at the CDS. The galactocentric distances in this table were estimated considering the geometric parameters inclination ($i = 74°$) and position angle ($\gamma = 170°$) given by Schaap et al. (2000).

Through a simple visual inspection in the optical HST images, we identified several candidates to HII regions. We characterized these as extended objects with diffuse emission in the studied bands ($F475W$, $F606W$ and $F814W$). We then detected 23 candidates, which are listed in Table 4, where we present their coordinates and approximate sizes.

We found a very good correlation between these regions and the PLC groups. We found that 18 HII candidates were related with one or more PLC groups. This fact suggests that most of the HII regions are probably powered by several massive stars, however the HII regions not correlated with a PLC group are probably being stimulated by a few sources that did not pass our PLC criteria ($p = 8$ stars).

5. Large-scale young stellar structures

As was mentioned above, young stellar groups exist in a wide variety of scales, from star clusters to stellar complexes, or

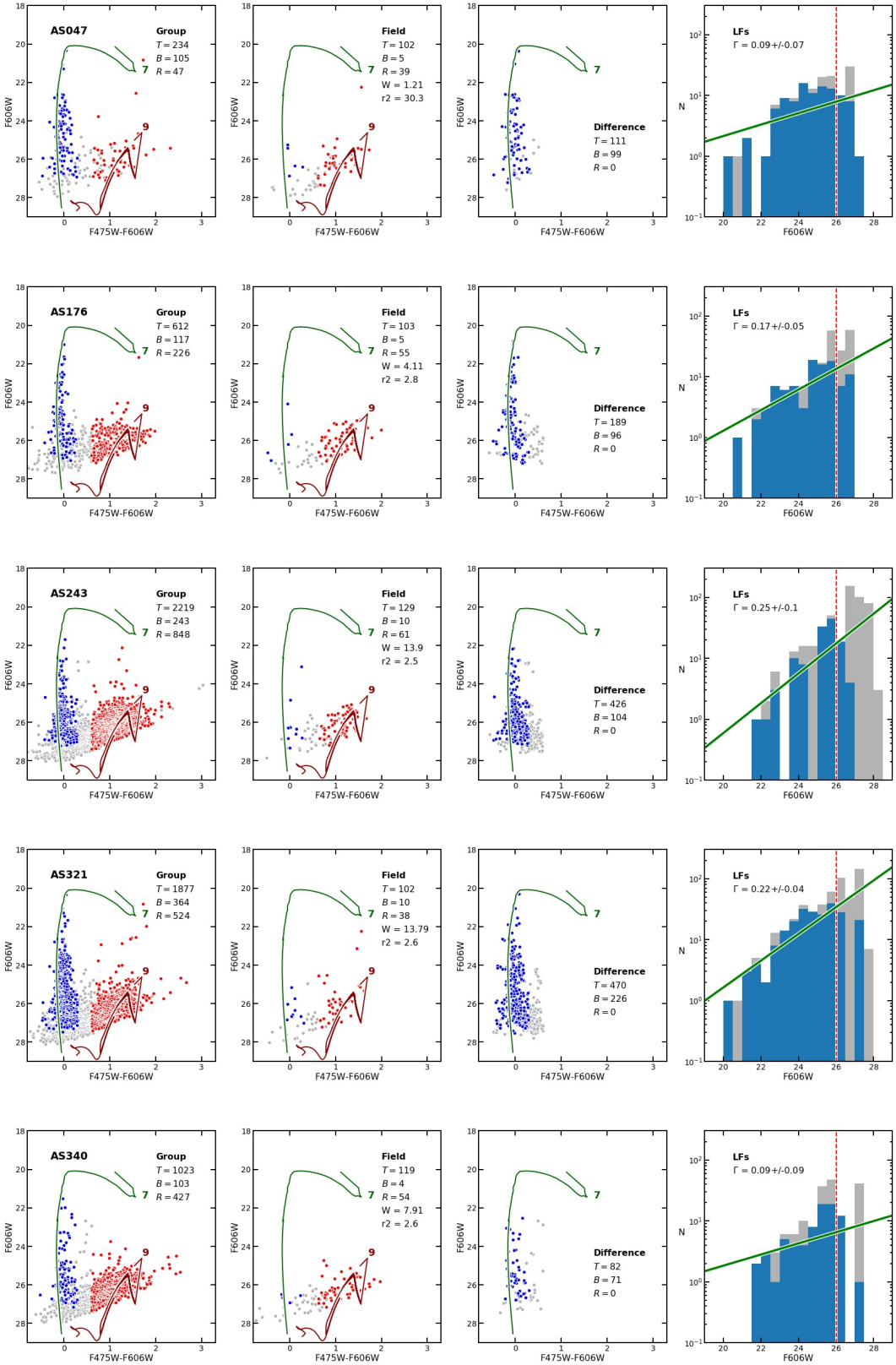

Fig. 7. Color magnitude diagrams for five selected young stellar groups. Each row presents from *left* to *right*: CMD for the group region, for its corresponding comparison field and the resulting difference. Blue and red symbols indicate selected blue and red objects, respectively. The curves indicate the 10^7 yr and 10^9 yr isochrones for solar metallicity ($Z = 0.0152$) from Tang et al. (2014) displaced according the adopted distance and reddening for NGC 247. The amount of total (T), blue (B) and red (R) stars are also presented. The values W and $r2$ indicate the weight and external radius of the field (see text), respectively. In the right panels, gray histogram is from all objects remaining after subtraction and the blue histogram is only for the blue population. The linear fit for brightest objects ($F606W < 26$, dashed line) and the obtained slope value (Γ) is shown.

Table 4. Candidates to HII regions.

ID	α_{j2000} [hh:mm:ss]	δ_{j2000} [dd:mm:ss]	Diameter [″]
1	00:47:13.38	−20:51:40.0	3.7
2	00:47:13.83	−20:52:16.6	0.9
3	00:47:13.29	−20:52:15.4	1.4
4	00:47:13.63	−20:51:16.0	2.2
5	00:47:08.81	−20:50:55.1	4.0
6	00:47:08.37	−20:50:30.2	1.2
7	00:47:08.40	−20:50:32.2	1.5
8	00:47:14.37	−20:50:08.2	2.0
9	00:47:12.17	−20:49:21.0	4.4
10	00:47:12.45	−20:49:07.3	3.2
11	00:47:10.21	−20:48:48.0	3.2
12	00:47:14.99	−20:48:38.6	3.0
13	00:47:15.74	−20:47:44.7	3.8
14	00:47:15.92	−20:47:40.5	1.5
15	00:47:05.79	−20:48:05.2	2.5
16	00:47:17.52	−20:47:26.6	1.0
17	00:47:15.78	−20:47:22.1	2.7
18	00:47:15.08	−20:46:07.6	5.2
19	00:47:07.59	−20:45:55.3	3.0
20	00:47:05.10	−20:45:19.8	1.5
21	00:47:03.45	−20:44:45.5	0.9
22	00:47:11.54	−20:44:26.3	5.5
23	00:47:12.43	−20:46:42.9	1.8

Notes. This table is available in electronic form at the CDS.

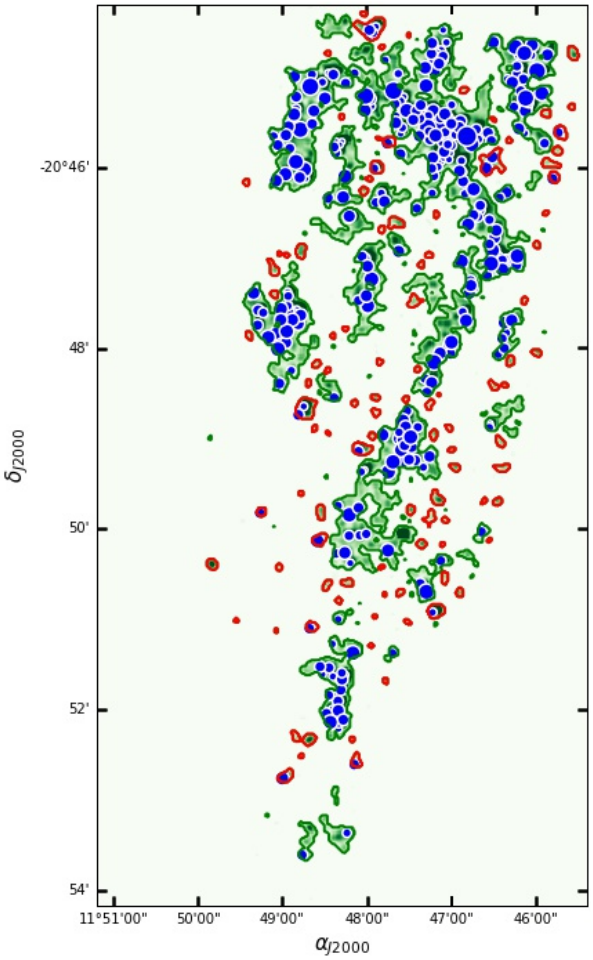

Fig. 8. Kernel density map of brightest blue stars in the studied region of NGC 247 obtained using a Gaussian kernel with a 2 arcsec bandwidth. Green and red levels indicate regions with and without hierarchical structure, respectively. Blue circles present the location of identified young stellar groups using PLC. The blue stars density map is available in electronic form at the CDS.

even larger structures. Several authors (e.g., Gouliermis 2018; Bastian et al. 2007) proposed that star formation occurs in a continuous fashion, characterized by an hierarchical pattern in which the star cluster and association are the denser inner part.

To identify larger young stellar structures, we constructed a surface stellar density map over the bright and blue stars of the NGC 247 studied region (see Sect. 3.1). This was performed using the kernel density estimation (KDE) method. That is, we convolved the stellar distribution with a Gaussian kernel. This method requires choosing a characteristic bandwidth for the kernel; this selection was done with an empirical approach. We first employed the stratified K-folds cross-validation and grid search methods to select the best parameters for an algorithm; in brief, a range of bandwidth values were tested over a sample of the data and we chose the value that produced a minor error. In our case, the bandwidth values ranged from 1 arcsec to 10 arcsec and a 20-fold test. These steps led to a minimum error bandwidth of 3 arcsec. Then, we built the corresponding stellar density map using this bandwidth value and lower values; we checked in all these maps that the main structures were still preserved and that these structures complemented those found using the PLC method. We finally adopted a bandwidth of 2 arcsec. The final adopted stellar density map of the bright blue stars is presented in Fig. 8. The minimum error bandwidth value estimation and KDE map construction were performed using, respectively, the GridSearchCV and KernelDensity tasks of the Python scikit-learn library (see Pedregosa et al. 2011[8]).

Several features were evident in the obtained stellar density map. In particular, we found the main overdensity at the galactic center, the NE-SW bar direction and the two main spiral arms in addition to a large number of smaller structures both inside and outside the main structures. In fact, the adopted 2 arcsec bandwidth corresponds to ∼35 pc (standard deviation) at the NGC 247 adopted distance and this size was the limit of resolved structures in the KDE map.

To identify structures in the young stellar population of NGC 247, we built the corresponding dendrograms of the KDE map using the core algorithm implemented in the astrodendro library in Python[9]. Basically, the generated dendrogram obtained from the KDE map is a "tree" type graphic diagram representing the skeleton of the map. In this representation, the "leaves" indicate the density peaks of the map and their joining represent the valleys (see Rosolowsky et al. 2008 for more details). The diagram follows until a minimum density threshold ($\rho_{\rm min}$) is reached. In order to avoid those peaks from noise fluctuation in the density map in the diagram, it is also necessary to indicate a minimum acceptable fluctuation ($\Delta\rho_{\rm min}$). After several tests with different pairs of these parameters, we adopted $\rho_{\rm min} = 0.12$ stars arcsec^{-2} and $\Delta\rho_{\rm min} = 0.01$ stars arcsec^{-2} since they produced clear dendrograms. This procedure allowed us to identify two kinds of overdensities (above $\rho_{\rm min}$): 28 with

[8] See https://scikit-learn.org for more details.

[9] See https://dendrograms.readthedocs.io/en/stable/ for details.

internal substructures (green levels in Fig. 8) and 102 without substructures (red ones in Fig. 8). The corresponding diagrams for the 15 most important structures (with more than 4 decendents) are presented in Fig. 9, where some relevant parameters of each remarked structure are also indicated. These large-scale structures complement the small-scale structures already found using the PLC method (see Sect. 3.2). Only 18 young stellar groups found by PLC are placed at overdensities without substructures. This represents a small percentage (~5%); similar percentages were found in other galaxies (e.g., Gouliermis et al. 2017; Efremov 1995). These few groups could be formed by different initial condition in the ISM, or perhaps they are older and their larger associated structures are too loose to be detected as overdensities in the density map.

6. Morphological analysis

Figures 8 and 9 reveal the presence of a hierarchical organization of the young stellar population, in which a structure with low stellar density may contain one or more substructures with higher stellar densities inside it. This hierarchical structure is considered typical in several star-forming regions and galaxies (e.g., Gouliermis 2018; Sun et al. 2018; Rodríguez et al. 2018; Gusev 2014), and could be inherited from their parent molecular clouds, which present a self-similar or fractal distribution (Elmegreen 1999). In fact, this fractal behavior is consistent with a scenario of star formation regulated by turbulence and self-gravity of the interstellar medium (ISM), in which the molecular cloud is fragmented in successive smaller clouds (Elmegreen & Efremov 1996).

We investigated the properties of the clustering in the young structures detected in Sects. 3 and 5. That is, we studied their corresponding fractal behavior using different methodologies. In the case of large-scale structures, we estimated the fractal dimension (D_2; Mandelbrot 1982) through the perimeter (P) area (A) relation and cumulative size (R) distribution. In the former case the relation $P \propto A^{D_2/2}$ (Falgarone et al. 1991; Sun et al. 2018) is verified, whereas in the latter, the following relation $\mathrm{d}N/\mathrm{d}\log(R) \propto R^{-D}$ (Mandelbrot 1982; Elmegreen & Falgarone 1996) is valid. The obtained values in each case were 1.58 ± 0.02 and 1.8 ± 0.2. These values are close to those reported for other star-forming regions, as well as for several galaxies, and agree with a scenario of hierarchical stellar formation in which newly born stars follow the gas distribution (Sun et al. 2017, 2018). In Fig. 10 we show both relations with their corresponding fractal dimension fits. In panel a, we can see that the structures with sizes under the resolution limit follow the perimeter area relation for a circle.

In the case of small structures, we computed the Q parameter introduced by Cartwright & Whitworth (2004) to distinguish between a smooth large-scale radial density gradient and multiscale fractal clustering. The Q parameter is defined as the ratio of two parameters: $\overline{m}$, which is the mean edge length in a minimum spanning tree (MST), normalized by the cluster area, and $\overline{s}$, which is the mean separation of the points, normalized by the cluster ratio. That is,

$$\overline{m} = \frac{1}{(AN)^{1/2}} \sum_{i=1}^{N-1} m_i$$

$$\overline{s} = \frac{2}{N(N-1)R_{sc}} \sum_{i=1}^{N-1} \sum_{j=i+1}^{N} \left| \boldsymbol{r}_i - \boldsymbol{r}_j \right|,$$

where N is the number of objects connected by the PLC, A is the area of the smallest circle that contains all the objects, $R_{\rm sc}$ is its corresponding radius, and r_i is the position of the i object. We found that $R_{\rm sc} \sim 0.8R$, where R is the adopted radius for the stellar groups computed in Sect. 4 and presented in Table 3.

To estimate $\overline{m}$, we constructed the MST of each stellar group, which is the shortest possible network that connects all the stars in the cluster and there are no closed loops. The MST was built using the minimum_spanning_tree task at Python scipy.sparse.csgraph library.

Cartwright & Whitworth (2004) obtained that values of Q greater than 0.8 correspond to a central concentrated distribution for artificial clusters, while smaller values agree with fractal structures. In this last case, Q values decreasing in the range 0.8–0.45 are related to a fractal dimension (D_2) decreasing from 2 to 0.5.

We computed then $\overline{m}$, $\overline{s}$, and Q for all groups detected in Sect. 3.2. We also evaluated their corresponding errors obtaining these values several times (~100 experiments) on each stellar group using the bootstrap method (Gregorio-Hetem et al. 2015) and computing the standard deviations of the different values computed on each experiment. The obtained results are in the last columns of Table 3 and represented in Fig. 11. In particular the computed errors values were $e_{\overline{m}} \sim 0.08$, $e_{\overline{s}} \sim 0.08$, and $e_Q \sim 0.10$. From Fig. 11 we notice that most of the Q values are lower than 0.8 and only a few are above this value, but they can be explained by the uncertainty of these values. Therefore it is possible to conclude that all the identified young stellar groups reveal a fractal structure. This fact could suggest that the young groups detected in the present work are very young and still show the distribution of their parent molecular clouds (Grasha et al. 2018; Sánchez & Alfaro 2010).

7. Conclusions

We performed an analysis of the young stellar population in the Sculptor group galaxy NGC 247. Through the PLC method we found 339 young stellar groups that could be open clusters, stellar associations, or a bit larger young groups.

We derived a catalog that contains the main characterizes of each group. For these groups we derived a mean radius of 60 pc and a mode in the size distribution between 30 and 70 pc. This values are a little larger than the radii found in the literature for most galaxies including our Galaxy. We also derived a mean density of 1.6×10^{-5} stars pc^{-3} computing stars brighter than $B1$. The LF slope distribution shows a bimodal shape with maximums at 0.1 and 0.2. This could be interpreted as the presence of two stellar population with different characterizations. The first value, which corresponds to the higher value in the distribution, represents flatter LF slopes. This population might be younger and so it would have more bright stars, causing the LF slope to become flatter. The second value is consistent with that found for NGC 253 and the Milky Way. We detected a list of HII region candidates finding an excellent correlation between the candidates and the PLC groups.

On the other hand, we studied the internal structure of each of the 339 PLC groups by means of the Q parameter. We obtained that the entire sample presents subclumpings. This fact suggests that the studied population is very young and the groups still preserve the same structure of the molecular clouds from which they form. This idea is supported by the flat values in the LF slope. The young groups are expected to evolve from a internal distribution with substructures to a more uniform distribution with time.

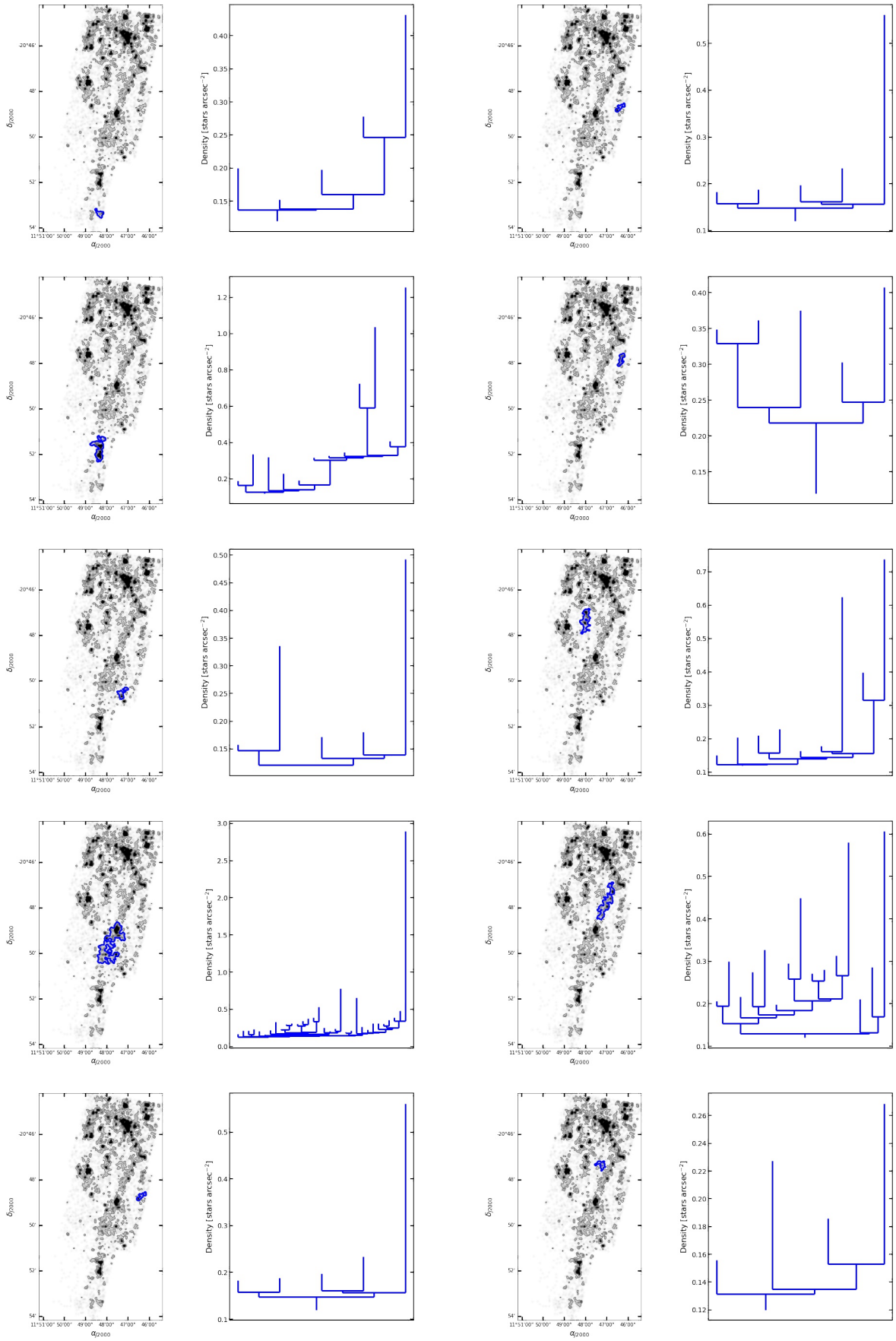

Fig. 9. Dendrograms of 15 main NGC 247 structures. The left panels identify in blue each structure over the KDE, whereas the right panels present the corresponding dendrogram.

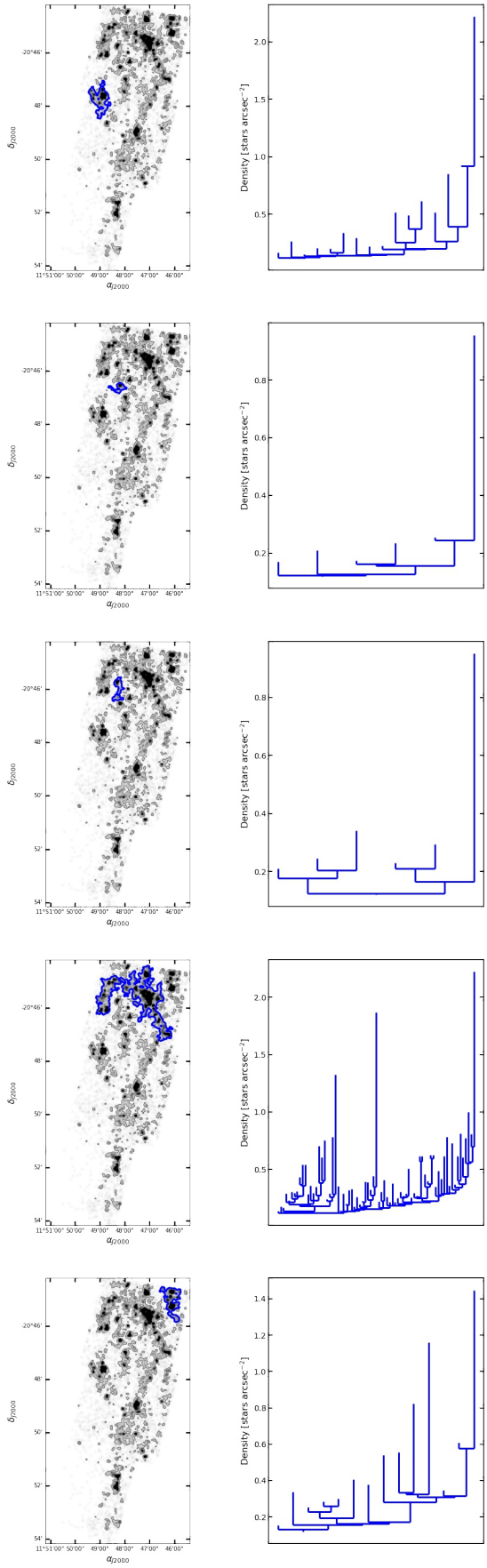

Fig. 9. continued.

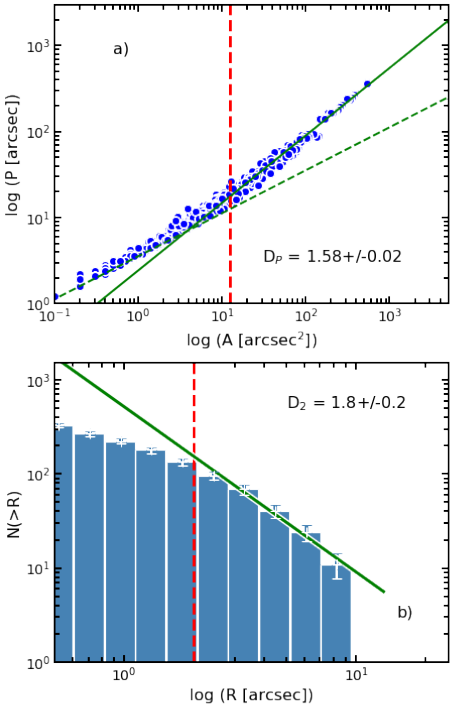

Fig. 10. Perimeter-area relation (*panel a*) and cumulative size histogram (*panel b*) for the young stellar structures detected in the density map. The vertical dashed lines indicate the resolution limit of the KDE map and solid line are the best fits following the behavior of large structures. Fractal dimension values obtained in each case are indicated. *Panel a*: dashed sloped line shows the relation for a circle ($P \propto A^{0.5}$). *Panel b*: errors are from $\sqrt{N}$.

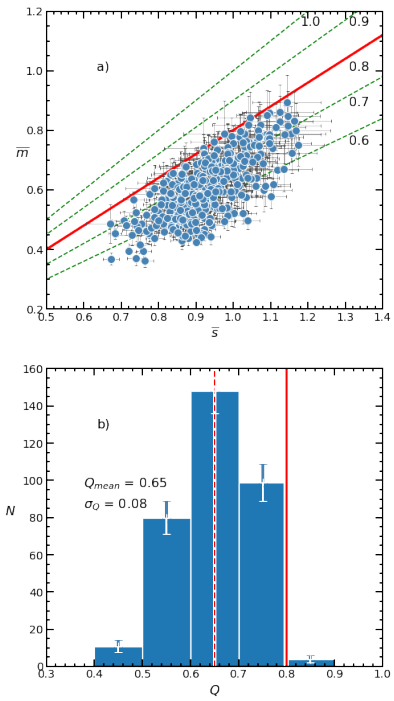

Fig. 11. *Panel a*: trend of $\overline{m}$ vs. $\overline{s}$ for the 339 PLC groups. Lines indicate the location for different Q values. Error bars are also presented. *Panel b*: Distribution of Q values. Red line indicates $Q = 0.8$. Error bars are computed as $\sqrt{N}$.

We detected larger young stellar structures through the blue stars density map. For these structures a high degree of clustering is revealed by the dendrograms shown in Fig. 9. By means of the perimeter-area relation and the cumulative size distribution for these structures we obtained fractal dimensions of 1.58 ± 0.02 and 1.8±0.2, respectively. These values are consistent with those obtained in other star-forming regions and galaxies and are consistent with a scenario of hierarchical star formation regulated by supersonic turbulence and self gravity.

We found a small percentage (∼5%) of the young star groups that do not seems to be part of the global hierarchical structure observed. This small percentage was also found in others galaxies and could be pointing to different initial conditions of the ISM when these groups form. Another possibility is that these groups are older and therefore their associated major structures have evolved into a loose population that is difficult to detect from background stars.

Acknowledgements. We thank the referee for helpful comments and constructive suggestions that helped to improve this paper. MJR and GB acknowledge support from CONICET (PIP 112-201701-00055). MJR is a fellow of CONICET. This work was based on observations made with the NASA/ESA *Hubble* Space Telescope, and obtained from the *Hubble* Legacy Archive, which is a collaboration between the Space Telescope Science Institute (STScI/NASA), the Space Telescope European Coordinating Facility (ST-ECF/ESA), and the Canadian Astronomy Data Centre (CADC/NRC/CSA). Some of the data presented in this paper were obtained from the Mikulski Archive for Space Telescopes (MAST). STScI is operated by the Association of Universities for Research in Astronomy, Inc., under NASA contract NAS5-26555. Support for MAST for non-HST data is provided by the NASA Office of Space Science via grant NNX09AF08G and by other grants and contracts. This research has made use of "Aladin sky atlas" developed at CDS, Strasbourg Observatory, France. We also made use of astrodendro, a Python package used to compute dendrograms of astronomical data (`http://www.dendrograms.org/`).

References

Bastian, N., Ercolano, B., Gieles, M., et al. 2007, MNRAS, 379, 1302
Battinelli, P. 1991, A&A, 244, 69
Battinelli, P., Capuzzo-Dolcetta, R., Hodge, P. W., Vicari, A., & Wyder, T. K. 2000, A&A, 357, 437
Baume, G., Vázquez, R. A., Carraro, G., & Feinstein, A. 2003, A&A, 402, 549
Blaauw, A. 1964, ARA&A, 2, 213
Carignan, C., & Puche, D. 1990, AJ, 100, 641
Cartwright, A., & Whitworth, A. P. 2004, MNRAS, 348, 589
Dalcanton, J., Williams, B., & ANGST Collaboration 2008, Space Sci. Proc., 5, 115
Davidge, T. J. 2006, ApJ, 641, 822
Dolphin, A. E. 2000, PASP, 112, 1383
Drazinos, P., Kontizas, E., Karampelas, A., Kontizas, M., & Dapergolas, A. 2013, A&A, 553, A87
Drazinos, P., Karampelas, A., Kontizas, E., et al. 2016, MNRAS, submitted [arXiv:1604.03165]
Efremov, Y. N. 1995, AJ, 110, 2757
Efremov, Y. N., & Elmegreen, B. G. 1998, MNRAS, 299, 588
Elmegreen, B. G. 1999, ApJ, 527, 266
Elmegreen, B. G., & Efremov, Y. N. 1996, ApJ, 466, 802
Elmegreen, B. G., & Falgarone, E. 1996, ApJ, 471, 816
Elmegreen, D. M., & Salzer, J. J. 1999, AJ, 117, 764
Falgarone, E., Phillips, T. G., & Walker, C. K. 1991, ApJ, 378, 186
Feinstein, C., Baume, G., Rodriguez, J., & Vergne, M. 2019, ArXiv e-prints [arXiv:1903.10989]
Ferguson, A. M. N., Wyse, R. F. G., Gallagher, III., J. S., & Hunter, D. A. 1996, AJ, 111, 2265
García-Varela, A., Pietrzyński, G., Gieren, W., et al. 2008, AJ, 136, 1770
Girardi, L., Barbieri, M., Groenewegen, M. A. T., et al. 2012, Astrophys. Space Sci. Proc., 26, 165
Gouliermis, D. A. 2018, PASP, 130, 072001
Gouliermis, D. A., Elmegreen, B. G., Elmegreen, D. M., et al. 2017, MNRAS, 468, 509
Grasha, K., Calzetti, D., Bittle, L., et al. 2018, MNRAS, 481, 1016
Gregorio-Hetem, J., Hetem, A., Santos-Silva, T., & Fernandes, B. 2015, MNRAS, 448, 2504
Gusev, A. S. 2014, MNRAS, 442, 3711
Kharchenko, N. V., Piskunov, A. E., Röser, S., et al. 2009, A&A, 504, 681
Kiss, L. L., & Bedding, T. R. 2005, MNRAS, 358, 883
Konstantopoulos, I. S., Smith, L. J., Adamo, A., et al. 2013, AJ, 145, 137
Lada, C. J., & Lada, E. A. 2003, ARA&A, 41, 57
Larsen, S. S. 1999, A&AS, 139, 393
Mandelbrot, B. B. 1982, The Fractal Geometry of Nature (New York: WH Freeman)
Melnik, A. M., & Efremov, Y. N. 1995, Astron. Lett., 21, 10
O'Donnell, J. E. 1994, ApJ, 437, 262
Olsen, K. A. G., Miller, B. W., Suntzeff, N. B., Schommer, R. A., & Bright, J. 2004, AJ, 127, 2674
Pedregosa, F., Varoquaux, G., Gramfort, A., et al. 2011, J. Mach. Learn. Res., 12, 2825
Phelps, R. L., & Janes, K. A. 1993, AJ, 106, 1870
Rodríguez, M. J., Baume, G., & Feinstein, C. 2016, A&A, 594, A34
Rodríguez, M. J., Baume, G., & Feinstein, C. 2018, MNRAS, 479, 961
Rosolowsky, E. W., Pineda, J. E., Kauffmann, J., & Goodman, A. A. 2008, ApJ, 679, 1338
Sánchez, N., & Alfaro, E. J. 2010, Lecture Notes and Essays in Astrophysics, 4, 1
Schaap, W. E., Sancisi, R., & Swaters, R. A. 2000, A&A, 356, L49
Schlafly, E. F., & Finkbeiner, D. P. 2011, ApJ, 737, 103
Sun, N.-C., de Grijs, R., Subramanian, S., et al. 2017, ApJ, 835, 171
Sun, N.-C., de Grijs, R., Cioni, M.-R. L., et al. 2018, ApJ, 858, 31
Tang, J., Bressan, A., Rosenfield, P., et al. 2014, MNRAS, 445, 4287
Tao, L., Feng, H., Kaaret, P., Grisé, F., & Jin, J. 2012, ApJ, 758, 85